



Optical coherence tomography angiography (OCT-A) in an animal model of laser-induced choroidal neovascularization

Johanna H. Meyer^{*}, Petra P. Larsen, Claudine Strack, Wolf M. Harmening, Tim U. Krohne, Frank G. Holz, Steffen Schmitz-Valckenberg

Department of Ophthalmology, University of Bonn, Bonn, Germany

ARTICLE INFO

Keywords:

OCT angiography
OCTA
Fluorescein angiography
Rat
Rodent
In vivo imaging
Retinal vascular plexus
Retinal vessel density

ABSTRACT

Aim of the study was to compare optical coherence tomography angiography (OCT-A) and conventional fluorescein angiography (FA) for quantitative analysis of the retinal and choroidal vasculature in the animal model of laser-induced choroidal neovascularization (CNV). Therefore, Dark Agouti rats underwent argon laser photocoagulation to induce CNV at D0. In vivo imaging using combined confocal scanner laser ophthalmoscopy (cSLO)-based FA and OCT-A (Heidelberg Engineering GmbH, Heidelberg, Germany) was performed before and immediately after laser treatment as well as at day 2, 7, 14 and 21. OCT-A en-face images were compared to cSLO images obtained by conventional FA topographic uptake recorded using a series of different pre-defined focus settings. For a quantitative comparison of CNV imaging by OCT-A and FA, CNV area, vessel density, number of vessel junctions, total vessel length and number of vessel end points were analyzed. Subsequent ex vivo analyses of the CNV included immunofluorescence staining of vessels in retinal and RPE/choroidal/scleral flatmount preparations. We found, that OCT-A allowed for high-resolution non-invasive imaging of the superficial, intermediate and deep retinal capillary plexus as well as the choroidal blood vessels in rats. Compared with OCT-A, visualization of CNV progression by invasive FA was less accurate, in particular the deep vascular plexus was visualized in more detail by OCT-A. The area of neovascularization was mainly detected in the deep retinal vascular plexus, outer nuclear layer (ONL), ellipsoid zone (EZ) and the choroid. Within the laser lesions, signs of CNV formation occurred at day 7 with progression in size and number of small vessels until day 21. Due to leakage and staining effects, CNV areas appeared significantly larger in FA compared to OCT-A images ($p \leq 0.0001$ for all tested layers). Vessel density, number of vessel junctions, total vessel length and number of vessel end points were significantly higher in intermediate vascular plexus (IVP) and deep vascular plexus (DVP) in OCT-A compared to FA images. Overall, CNV area in flatmounts was similar to OCT-A results and much smaller compared to the area of dye leakage by FA. This study demonstrates that in vivo OCT-A imaging in small animals is feasible and allows for precise analysis of the formation of new blood vessel formation in the animal model of laser-induced CNV. Given its superior axial resolution, sensitivity and non-invasiveness compared to conventional FA imaging, OCT-A opens the door for a more detailed evaluation of CNV development in such a model and, thus, enables the analysis of the response to novel therapeutic interventions in longitudinal in vivo studies.

1. Introduction

In the last decade, advances in ophthalmological in vivo imaging techniques have improved the pathophysiological understanding of various retinal and choroidal diseases. Already well-established diagnostic tools including spectral-domain optical coherence tomography (SD-OCT) and confocal scanning laser ophthalmoscopy (cSLO) have improved clinical care of patients with retinal diseases. With the development of OCT-angiography (OCT-A), the non-invasive and spatial

visualization of retinal and choroidal vascular structures by recording blood motion contrast has become possible (Spaide et al., 2015). This diagnostic imaging modality allows for non-invasive three-dimensional visualization of retinal as well as choroidal vascular structures with higher resolution and accuracy and without prior invasive fluorescent dye injection (Fang et al., 2016). Retinal and choroidal vascular abnormalities are key manifestations in several blinding eyes diseases, including diabetic retinopathy, retinal vein occlusions and choroidal neovascularization due to age-related macular degeneration and other

^{*} Corresponding author. Universitäts-Augenklinik Bonn, Ernst-Abbe-Str. 2, 53127, Bonn, Germany.

E-mail address: Johanna.Meyer@ukbonn.de (J.H. Meyer).

<https://doi.org/10.1016/j.exer.2019.04.002>

Received 26 October 2018; Received in revised form 18 March 2019; Accepted 4 April 2019

Available online 16 April 2019

0014-4835/ © 2019 The Authors. Published by Elsevier Ltd. This is an open access article under the CC BY-NC-ND license

(<http://creativecommons.org/licenses/by-nc-nd/4.0/>).

etiologies. The advent of clinically applicable anti-VEGF (anti-vascular endothelial growth factor) therapies is only the “tip of the iceberg” of future additions to the clinical armamentarium to effectively treat vascular eye diseases. The precise and detailed visualization of the retinal and choroidal vascular network appears mandatory for monitoring treatment effects in these conditions.

OCT-A can also be performed in various animals and animal models of retinal diseases (Alnawaiseh et al., 2016; Atzpodien et al., 2015; Augustin et al., 2018; Kim et al., 2018; Leahy et al., 2015; Liu et al., 2015; Meyer et al., 2017; Nakagawa et al., 2018; Park et al., 2016; Shah et al., 2016; Soetikno et al., 2017; Srinivasan and Radhakrishnan, 2013; Uehara et al., 2018). In 2015 Leahy et al. demonstrated an in-depth analysis of the (untreated) rat retinal vascular network by combined OCT-A microscopy and Doppler OCT technique (Leahy et al., 2015). In addition, Giannakaki-Zimmermann et al. showed a more refined quantification of the deep vascular plexus by OCT-A compared to conventional fluorescein angiography (FA) and confocal microscopy of retinal flatmounts in albino BALB/c and *rd2* mice (Giannakaki-Zimmermann et al., 2016). However, the laser-induced choroidal neovascularization (CNV) model as a common animal model for neovascular age-related macular degeneration (AMD) has been hardly studied with OCT-A commercially available standard devices until now. The CNV is generated by a focal rupture of Bruch's membrane using laser photocoagulation (Dobi et al., 1989). During its development, formation as well as progression of the neovascular network extending across various retinal and choroidal layers can be observed (Fig. 1). This model has been extensively investigated in vivo by funduscopy, cSLO or OCT imaging and ex vivo using immune- or fluorescence-stained cross sections or flatmount preparations in different animal models (Goody et al., 2011; Hoerster et al., 2012; Lambert et al., 2013; Paques et al., 2010; Wigg et al., 2015). To the best of our knowledge, a characterization and quantification of the different rat retinal and choroidal vascular structures in the animal model of laser-induced CNV by OCT-A in rats has not been evaluated in detail or directly compared with FA or ex vivo preparations yet. Furthermore, the number of animal studies with quantitative OCT-A assessment with commercially available devices is low.

The aim of the current study was to investigate the feasibility of OCT-A in a rat model of laser-induced CNV and to compare its performance with conventional FA and ex vivo examination of retinal as well as RPE/choroidal/scleral flatmounts by confocal fluorescence microscopy.

2. Material and methods

2.1. Animals

All animal procedures were approved by local authorities (local ethics committee “Landesamt für Natur, Umwelt und Verbraucherschutz Nordrhein-Westfalen”) and complied with the Association for Research in Vision and Ophthalmology (ARVO) statement for the Use of Animals in Ophthalmic and Vision Research. Experiments were performed with adult Dark Agouti rats (Janvier Labs, Rennes, France), each weighing 200–250 g. Rats ($n = 16$) were anesthetized for all procedures by intraperitoneal injection of ketamine (60 mg/kg body weight) and medetomidine hydrochloride (0.5 mg/kg body weight) as previously described (Cunea et al., 2014; Meyer et al., 2014, 2016, 2017). Anesthesia of rats was reversed by intraperitoneal injection of a 20% atipamezol (1 mL/kg) solution. Animals received a topical administration of 0.5% tropicamide (Mydriaticum Stulln, Pharma Stulln, Stulln, Germany) eye drops for pupillary dilation of both eyes before in vivo imaging as well as laser treatment. Imaging was followed by topical administration of Corneregel (Corneregel, Bausch & Lomb, Berlin, Germany).

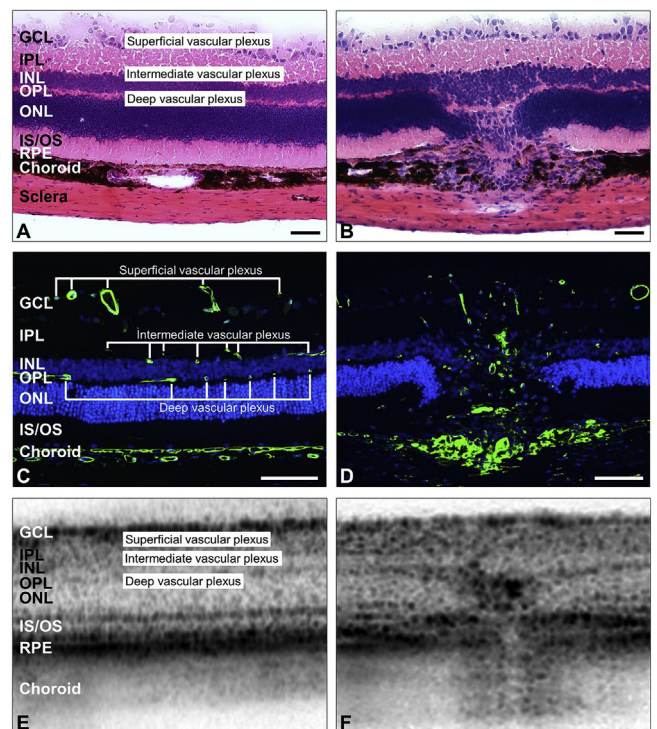


Fig. 1. Morphology and vascular plexus of the rat retina. H&E stained frozen section of an untreated (A) and a rat eye with a laser lesion (B, 14 days following the initial laser treatment) (scale bars: 50 μ m). The retinal capillary network consists of 3 different plexus: superficial (from RNFL to IPL), intermediate (from IPL to INL) and deep (INL to OPL) vascular plexus. The paraffin sections show an untreated eye (C) and a rat eye with a central laser spot (D, 14 days following the laser coagulation) (scale bars: 100 μ m). Both sections were stained with DAPI (blue) and isolectin B4 (green) for endothelial cells. OCT-B scans of an untreated (E) and a laser treated rat eye (F, 14 days following the laser treatment). The different morphological layers and retinal vascular plexus are indicated in E. (Abbreviations: RNFL = retinal nerve fiber layer; GCL = ganglion cell layer; IPL = inner plexiform layer; INL = inner nuclear layer; OPL = outer plexiform layer; ONL = outer nuclear layer; IS/OS = inner and outer segment; RPE = retinal pigment epithelium).

2.2. Laser photocoagulation

Retinal laser lesions (Fig. 1) were generated at day 0 (DO) to induce CNV formation as previously described (Meyer et al., 2014, 2016). An argon laser (Novus 2000, Coherent, Dieburg, Germany) with a slit lamp laser delivery system was used for photocoagulation with the following settings: 514 nm excitation, 1 s pulse duration, 150 mW laser power and 100 μ m spot size. In all eyes, a series of 5–6 laser lesions were concentrically placed around the optic nerve head and between retinal vessels. Successful disruption of Bruch's membrane was confirmed by formation of a bubble at the site of laser application immediately visualized with the slit lamp. Lesions with significant subretinal hemorrhage following the laser treatment were excluded ($n = 1$).

In two eyes of dark agouti rats, laser photocoagulation was set below threshold and no CNV was subsequently induced. Therefore, a 514 nm excitation, 0.1 s pulse duration, 50 mW laser power and a 100 μ m spot size setting was used. No bubble formation was observed during the laser application with the slit lamp indicating an unsuccessful CNV induction and only a chorioretinal burn was visualized (Supplement figure S1).

2.3. OCT-angiography

In vivo imaging in rats was conducted before and directly after laser treatment as well as at day 2, 7, 14 and 21 following laser coagulation.

For OCT-A, an OCT-A device (Spectralis prototype, Heidelberg Engineering, Heidelberg, Germany, software version SP-X1601) was used in the high resolution mode as described previously (Meyer et al., 2017). According to the protocol, anesthetized animals were placed on a customized platform in front of the camera lens. A 55° lens was used for cSLO and OCT-A imaging. Rigid rat contact lenses (micro-rat lens, radius: 2.70, diameter: 5.20, Cantor & Nissel Limited, Brackley, Northamptonshire, United Kingdom) and lubricating eye drops (Oculotect fluid 50 mg/mL, Novartis Pharma, Nürnberg, Germany) were used to prevent cataract formation and to optimize image clarity during OCT-A or FA imaging, respectively (Meyer et al., 2014, 2017). For OCT-A imaging, the length of the OCT reference arm was adjusted to the rat eye in the Spectralis OCT-debug window reaching 29,000 till 31,000 μm . Depending on the area involvement of the applied laser spots, the size of the scan field was adjusted by using one of three different volumes ($20^\circ \times 20^\circ$, $25^\circ \times 25^\circ$ and $25^\circ \times 55^\circ$) with 350 till 651 horizontal OCT-A-B-scans (depending on the size). Based on a full-spectrum amplitude decorrelation algorithm, 25 sequential frames were used for the calculation of one B-scan and the distance between two single B-scans was set to 11 μm . A focus setting of +17.25 diopter was selected for all eyes.

OCT-A en-face images were compared to cSLO images obtained by conventional FA. For analysis of OCT-A images, the following seven retinal and choroidal layers were segmented (Fig. 2): (1) superficial vascular plexus (SVP), (2) intermediate vascular plexus (IVP), (3) deep vascular plexus (DVP), (4) outer nuclear layer (ONL), (5) ellipsoid zone (EZ, containing the inner and outer segments of the photoreceptors), (6) inner choroid (IC) and (7) outer choroid (OC). OCT-A segmentation was performed semi-automatically by selecting the inner limiting membrane (ILM) followed by manually shifting segmentation of all seven layers in a standardized method (Fig. 2).

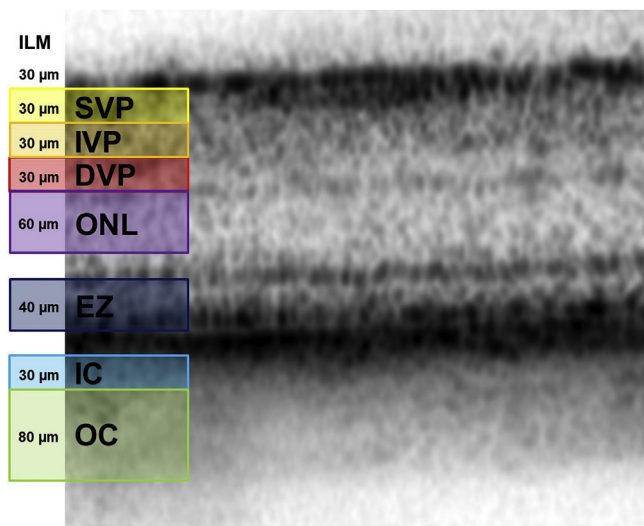


Fig. 2. Segmentation was performed automatically by selecting the inner limiting membrane (ILM) followed by manually shifting segmentation of 7 layers in a standardized method: the superficial vascular plexus (SVP) was segmented from 30 μm below the ILM to 60 μm below the ILM, followed by the intermediate vascular plexus (IVP) (30 μm), the deep vascular plexus (DVP) (30 μm), the outer nuclear layer (ONL) (60 μm) and the ellipsoid zone (EZ, 40 μm). Below the RPE the inner choroidal (IC) layer (30 μm) and the outer choroidal (OC) layer (80 μm) were segmented. Overall, the actual size of the highlighted segments and their allocation to different retinal layer is based on estimations, taking into account the limited resolution of in vivo imaging and the correlation to histology. For example, the actual size of the EZ would be considered to be much narrower by histology as shown here.

2.4. Fluorescein angiography using confocal scanning laser ophthalmoscopy

Near-infrared reflectance and fluorescence imaging (using the FA-mode) of the ocular fundus of both eyes was performed using cSLO (HRA2, Heidelberg Engineering, Heidelberg, Germany) in a single and standardized session as described previously (Meyer et al., 2014, 2016, 2017). Anesthetized animals were placed on a customized platform in front of the 55° camera lens. Imaging with the cSLO was performed in the high resolution mode with a mean image out of a series of single normalized images (15 frames) before and at predefined time points (2, 7, 14 and 21 days) following the initial laser treatment. The confocal approach allows for the acquisition of sectional scans through the rodent retina and investigates the depth location of fluorescent signals (Schmitz-Valckenberg et al., 2008, 2010). For FA, each animal underwent serial intravenous injection of 10% fluorescein dye (dose: 50 mg/kg body weight, Fluorescein Alcon, Alcon Pharma GmbH, Freiburg, Germany) (0.2 mL) and topographic uptake was recorded using different focus settings (+16, +14, +12, +10, +8, +6, +4, +2, 0, -4 and -8 diopter) in order to compare different fluorescence intensities. Angiograms were recorded immediately and until 10 min following the intravenous dye injection.

2.5. In vivo image analysis

The CNV area (laser lesion size) imaged with OCT-A and FA was quantified by two independent investigators (authors JM and PL). Therefore, images were analyzed with the help of an automated image-software provided by the system manufacturer (Heidelberg Eye Explorer, version 1.9.10.0, 2014, Heidelberg Engineering GmbH, Heidelberg, Germany) by selecting the area of CNV for all tested layers, laser spots and days (Supplement figures S2-S8). The laser lesion size of both investigators was averaged for all examined animals to calculate the overall CNV area and standard deviation. Scale values in both imaging modalities (HRA2 and OCT-A Spectralis prototype) are standardized for the human eye. To date no exact scaling for cSLO imaging for the eye of (dark Agouti) rats has been established. A rough estimation would be that the size of the average rat optic disc corresponds to 0.041 mm^2 (Maass et al., 2007; Meyer et al., 2014). For the analysis of the CNV area, the size of each CNV area was calculated in relation to the size of the optic nerve head of each individual rat eye and then analyzed for each layer and day. A single Bland-Altman plot for OCT-A and FA was used to evaluate the agreement between the two independent readers (Bland and Altman, 1999).

Furthermore, the retinal vascular network was analyzed by AngioTool (Zudaire et al., 2011) software (center for cancer research, version 0.6a, 64 bits, October 2014) as a plugin of Fiji (ImageJ 1.48v, Wayne Rasband, National Institute of Health, Bethesda, USA). An exemplary AngioTool output is shown in Fig. 5 in which the outline of the vessels is indicated in yellow, the skeleton in red and the branching points in blue. Before using AngioTool to assess the retinal vascular plexus, the OCT-A and FA images of the SVP, IVP as well as DVP were transformed to equal sizes by Fiji covering the area of laser lesions. The average number of visualized retinal vessels was calculated as vessel density indicating the percentage of area occupied by vessels inside the explant area in OCT-A and FA images (Zudaire et al., 2011). In addition, the number of vessel junctions, total vessel lengths and total number of vessel end points in the area of CNV were analyzed separately for the SVP, IVP and DVP for OCT-A and FA images.

2.6. Ex vivo measures and histology

For immunohistochemical analyses, both eyes underwent laser treatment (at D0). Following in vivo imaging procedure at day 21, all animals ($n = 16$) were euthanized applying 100% carbonic acid gas. Eyes were immediately enucleated and processed for frozen, paraffin sections or retinal and RPE/choroidal/scleral flatmount preparation

and examined by fluorescence microscopy as previously described (Meyer et al., 2014, 2016).

For additional light microscopically examination of frozen sections (Fig. 1 A and B), eyes at day 14 were processed immediately after in vivo imaging by embedding in OCT medium (Tissue Tek, Sakura Finetek Europe B.V., Alphen aan den Rijn, the Netherlands) on dry ice and stored at -80°C till needed. Frozen sections (Fig. 1 A and B) of $10\ \mu\text{m}$ were mounted on a glass slide, fixed with 100% methanol and stained with haematoxylin and eosin (H&E). H&E stains were investigated at $10\times$ or $20\times$ magnification with a light microscope (Olympus B \times 50; Olympus, Hamburg, Germany).

In brief, for immunofluorescence staining of $5\ \mu\text{m}$ thick serial sections paraffin sections of the eyes (Fig. 1 C and D), sections were mounted on a glass slide and labeled with DAPI (DAPI BioChemica, 4',6-Diamidino-2-phenylindole dihydrochloride, AppliChem GmbH, Darmstadt, Germany) and isolectin B4 (I21411, AlexaFluor488 conjugated, Life technologies, Eugene, Oregon, USA). All fluorescent images of paraffin sections were collected from fluorescence microscope (Leica MP S60, Leica Microsystems CMS GmbH, Mannheim, Germany) using a X10 objective and LAS v3.8.

For flatmount preparation, following enucleation and fixation, the anterior part of the eye was removed and the retina as well as the choroid were separated. Flatmount sections were incubated with a 1:100 dilution of isolectin B4 (I21411, Alexa488 conjugated, Life technologies, Eugene, Oregon, USA) for 2 h at room temperature. All fluorescent images of retinal and RPE/choroidal/scleral flatmounts were collected from an upright Leica TCS SP8 laser scanning confocal microscope with acousto-optical beam splitter (Leica TCS SP8; Leica Mikrosysteme Vertrieb GmbH, Wetzlar, Germany) using a $10\times$ objective and a solid-state laser for 488 nm. An image z-stack was recorded for each lesion and ex vivo CNV area was measured in retinal and RPE/choroidal/scleral flatmounts using ImageJ software.

The mean CNV area in flatmounts was calculated and compared with OCT-A and FA results at D21. In addition, grayscale images of OCT-A, FA and confocal microscopy of flatmount preparations were pseudo-colored according to SVP (red), IVP (green) and DVP (blue) and an overlay of these images was generated using ImageJ software (ImageJ 1.48v, Wayne Rasband, National Institute of Health, Bethesda, USA) (Haefliger et al., 2017).

2.7. Statistical analysis

Statistical analyses were performed by using the SPSS software package Statistics 25 (SPSS Inc., Chicago, IL, USA). All results were expressed as mean values \pm standard deviation (SD). Comparison of mean CNV area (in mm^2) between OCT-A and FA was performed using the Wilcoxon signed rank test. Statistical analysis of vessel density, number of vessel junctions, total vessel lengths and total number of vessel end points within the laser spot were performed using Wilcoxon signed rank test. Bland-Altman plots (Bland and Altman, 1999) were used to assess the inter-grader-reliability of the CNV area in OCT-A and FA images by two independent readers. Comparison of mean CNV area between OCT-A and histology as well as FA and histology was performed using Wilcoxon signed rank test. *P* values less than 0.05 were considered as statistically significant and significance levels are indicated using * for *P* less than or equal to 0.05, ** for *P* less than or equal to 0.01 and *** for *P* less than or equal to 0.001.

3. Results

3.1. In vivo imaging

High-resolution visualization of the untreated three retinal vascular plexus and the choroidal blood vessels was achieved by non-invasive OCT-A imaging (Fig. 3). In addition, avascular layers including ONL and EZ were illustrated. Visualization of the retinal and choroidal

vascular structures as well as the focal laser lesions was possible for all tested days and layers. At initial in vivo imaging (D0, prior to laser treatment), normal retinal and choroidal vessel structures were detectable. Immediately following photocoagulation, signs of edema were visible at the site of the laser lesions. Swelling in and around the laser spot was observable at day 2 (Fig. 3) whereas appearance of early CNV formation was detectable at day 7 with progression in structure, size and number of new blood vessels until day 21 (Fig. 3). Signs of new blood vessels were visible especially in the DVP, ONL, EZ as well as inner choroid (Fig. 3). Particular in the ONL and EZ, a subtle neovascular capillary network was identified in OCT-A images at day 14 and 21 (Figs. 3, 5 and 7). No distinct changes or vessel formation were detected in the SVP at all time points (Figs. 3–5). In the outer choroid, a bright inner circle within the laser lesion was often visualized in the first 2 weeks following laser treatment (Fig. 3). This circle vanished overtime and at day 21 following the laser photocoagulation, a hyporeflective spot remained. In general, some projection artefacts in OCT-A of the main retinal vessels in the SVP were identified in almost all deeper layers like IVP and DVP as well as ONL, EZ and IC (Figs. 3, 8 and 9). Motion artefacts were almost negligible in the narcotized animal. Laser photocoagulation below the threshold to induce CNV in the rat model showed in OCT-A images minor structural changes in the ONL, EZ and inner as well as outer choroid but no neovascular vessel formation (Supplement figure S1). In addition, no fluorescein leakage was detectable in FA in these eyes (Supplement figure S1).

With FA, the vascular network of the eye was imaged confocally using the cSLO technique. This allowed for monitoring of fluorescein leakage at the CNV site in vivo (Fig. 3). At the same time, the dye leakage obscured the detailed neovascular structures in the retina and choroid (Figs. 3–5 and 7). Leakage was detectable at day 2 following the initial laser photocoagulation in all retinal and choroidal layers with progression in structure and size till day 21.

Overall, OCT-A imaging was performed before FA. If the order of sequential imaging was changed to initial FA and then followed by OCT-A acquisition, no influence or difference in OCT-A image quality was observed by prior dye application. Due to leakage and staining effects, CNV area was in general much more prominent and larger in FA images compared to OCT-A images while OCT-A images revealed detailed structural changes (Figs. 3 and 4).

3.2. Quantitative analysis of CNV lesions

Quantitative analysis (Fig. 4) revealed that CNV size was significantly smaller (about twice or even three times smaller) in OCT-A images compared to FA images for all tested layers and days ($P \leq 0.0001$, Wilcoxon test). The size of the CNV area peaked at day 2 (D2) following the initial laser treatment in OCT-A as well as in FA images in all tested layers (Fig. 4). Almost no detectable CNV in the SVP was measured by OCT-A at all investigated time points. Measured values of the CNV area were largest for the inner and outer choroid in FA images and for the ONL and EZ in OCT-A images (Fig. 4). An overall decrease of the total CNV area was examined for all layers from day 2 until day 21 (Fig. 4) in OCT-A and FA images. Quantitative analysis of the CNV lesion size in OCT-A (Supplement figure S9) and FA (Supplement figure S10) images carried out by two independent investigators showed a good agreement between the readers.

3.3. Retinal vascular network structure assessment

In total, the overlay of the output of the retinal network examination with the software AngioTool and OCT-A images showed a good agreement (Fig. 5). In FA images, dye leakage covered the neovascular complex especially in the IVP as well as DVP resulting in a poor correlation with the software output (Fig. 5). Without initial laser treatment (marked as before, prior to laser treatment), vessel density for OCT-A and FA in the SVP as well as IVP were similar but OCT-A showed

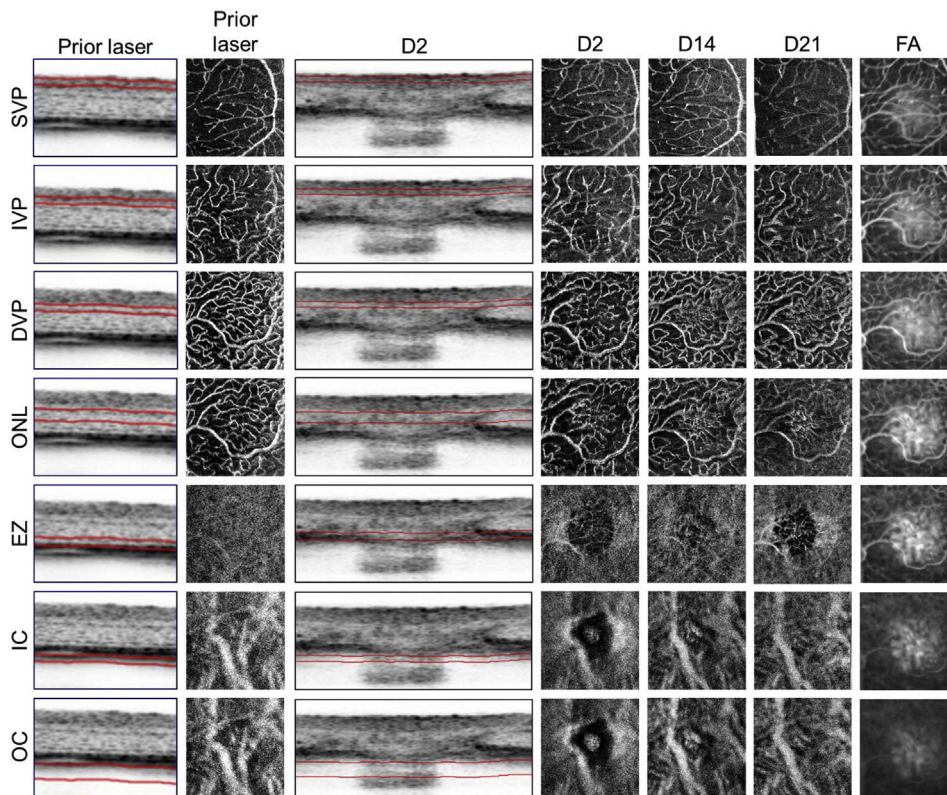


Fig. 3. In vivo imaging of a laser lesion by OCT, OCT-A and FA. OCT-A imaging of a laser lesion with the different observed layers in the rat eye over time following the laser treatment. Time points are indicated above the respective images (D = day following initial laser treatment). At D2, signs of edema and swelling of the tissue as effect of the laser treatment were visualized but no new blood vessels were observed. Early CNV formation was detectable at D7 (data not shown) with progression in size and structure until D21. Especially in deeper layers - like DVP, ONL and EZ - signs of new blood vessels were visible at D14 and D21. A subtle capillary network in the ONL and EZ was identified 21 days following the initial laser treatment. In FA (last row, at D21), neovascular structures were obscured by dye leakage and staining of the surrounding tissue.

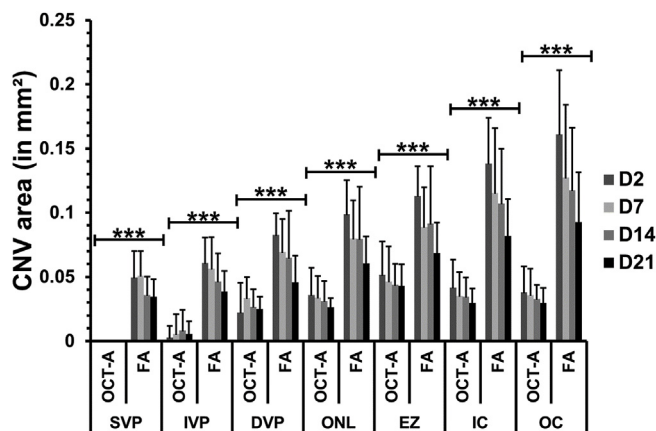


Fig. 4. Assessment of the CNV area. Analysis of the area of CNV (in mm²) for OCT-A (n = 18) and FA (n = 20) following the laser treatment over time (D = day following initial laser treatment). In the SVP, rarely no detectable CNV was measured by OCT-A at all investigated time points. Due to leakage and staining effects, CNV area was in general much more prominent and larger in FA images compared to OCT-A images while OCT-A images revealed detailed structural changes. A significant smaller CNV area was measured by OCT-A compared with FA for all time points and layers. Values of the CNV area were largest for the outer choroid in FA images and for the EZ in OCT-A images. Overall, the size of the CNV area decreased overtime. (***) $P < 0.001$, Wilcoxon signed rank test comparing CNV area in OCT-A and FA).

a higher vessel density in the DVP compared to FA. In both imaging modalities, vessel density (Fig. 5) in the SVP was comparable for all tested days following the laser treatment. Following the laser treatment, vessel density increased in the IVP and DVP in OCT-A images compared to the amount measured at D0 over time. In FA images, vessel density for SVP and IVP showed no significant difference compared to vessel density at D0. But a significant decrease in vessel density was observed in the DVP in FA (Fig. 5). In the deeper retinal vascular layers (IVP and

DVP) significant higher vessel density was measured for OCT-A compared to FA at D7, D14 and D21 (SVP: $P = 0.001$; IVP and DVP: $P < 0.0001$, Fig. 5).

The number of vessel junctions (Fig. 6 A), total vessel length (Fig. 6 B) and number of vessel end points (Fig. 6 C) increased from SVP to IVP and from IVP to DVP in OCT-A and FA images. In total, a significantly higher number of junctions ($P < 0.0001$ for SVP, IVP and DVP), total vessel length ($P = 0.001$ for SVP and $P \leq 0.0001$ for IVP as well as DVP) and number of vessel end points ($P \leq 0.0001$ for SVP, IVP and DVP) were seen by OCT-A compared to FA (Fig. 6). Overall, a slight increase in vessel density, number of vessel junctions, total vessel length and number of vessel end points was observed in the IVP and DVP for OCT-A and FA over time (Figs. 5 and 6).

3.4. Histology

In frozen and paraffin sections, CNVs were found to extend from the choroid into the subretinal space causing a local displacement of various retinal layers (Fig. 1). The EZ and ONL were shifted to superior layers and the OPL as well as the INL to inferior levels in the region of the laser lesion (Fig. 1).

The laser treated rat retinal capillary network could be immunohistochemically stained and quantified (Fig. 7). Immunohistochemistry of retinal and RPE/choroidal/scleral flatmounts was performed 21 days following the initial laser treatment. Ex vivo analysis showed new vessel formation within the center of laser lesions in retinal and RPE/choroidal/scleral flatmounts stained with Alexa488 conjugated isolectin B4 (Fig. 7). Clear neovascular vessel formation was detected in retinal flatmounts in the region comparable to the DVP, ONL and EZ (Fig. 7).

In vivo results by FA and OCT-A were correlated with confocal microscopy images and the CNV area of all three imaging modalities was calculated (Fig. 7). In total, CNV area in retinal and RPE/choroidal/scleral flatmounts was similar to OCT-A results and smaller compared to the area of dye leakage by FA. The differences in CNV size

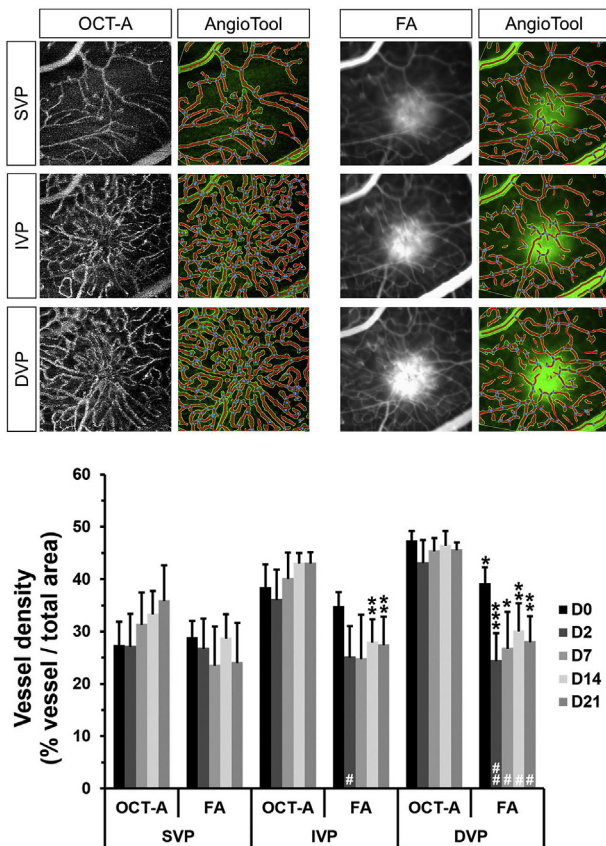


Fig. 5. Quantitative analysis of the vessel density. The retinal vascular network in the CNV area was analyzed by AngioTool software. The average number of visualized retinal vessels, the total vessel length, number of vessel end points and number of junctions were measured separately for the SVP (first row), IVP (second row) and DVP (third row) in the laser spot area for OCT-A (left columns, n = 18) and FA (right columns, n = 20) 14 days following the laser treatment (D14). The AngioTool output is shown in the corresponding right column, in which the outline of the vessels is indicated in yellow, the skeleton in red and the branching points in blue. Analysis of the mean linear vessel density (as the ratio of percentage of vessels and total area) at different time points (different time points are highlighted by different grey values – see legend on the right) between OCT-A and FA, shown separately for the three retinal vascular plexus (SVP, IVP and DVP). Statistical analysis using the Wilcoxon signed rank test showed significance of vessel density at all time points between OCT-A and FA for the DVP (shown by * P < 0.05; **P < 0.01; ***P < 0.001). For IVP, significance was additionally found at day 14 and day 21. Comparing vessel density to before laser treatment, significant differences in vessel density were identified at D2 for IVP and day 2, day 7, day 14 and days 21 for DVP, respectively (shown by #: P < 0.05; ##: P < 0.01).

measured in mm² for the three imaging modalities were calculated using the Wilcoxon signed rank test (OCT-A versus histology: SVP: not significantly different; IVP: not significantly different; DVP: P ≤ 0.001; ONL: P ≤ 0.0001; EZ: not significantly different; IC: P = 0.006; OC: P ≤ 0.001. FA versus histology: SVP: P ≤ 0.0001; IVP: P ≤ 0.0001; DVP: P = 0.03; ONL: P = 0.023; EZ: P ≤ 0.001; IC: P ≤ 0.0001; OC: P ≤ 0.0001). Almost no sign of CNV formation was detected in the ex vivo preparations for the SVP and only a minor area was affected in the IVP. This finding was comparable to the OCT-A results (Fig. 7). CNV area was largest in the ONL in retinal flatmounts and the size decreased towards the choroid.

Direct comparison between OCT-A, FA and confocal microscopy of retinal flatmount images in intact (Fig. 8) and laser treated (Fig. 9) rat retinae showed a reliable segmentation for OCT-A and confocal microscopy images. In FA, segmentation of the different retinal vascular plexus was less reliable and the overlays (Figs. 8 and 9) indicated

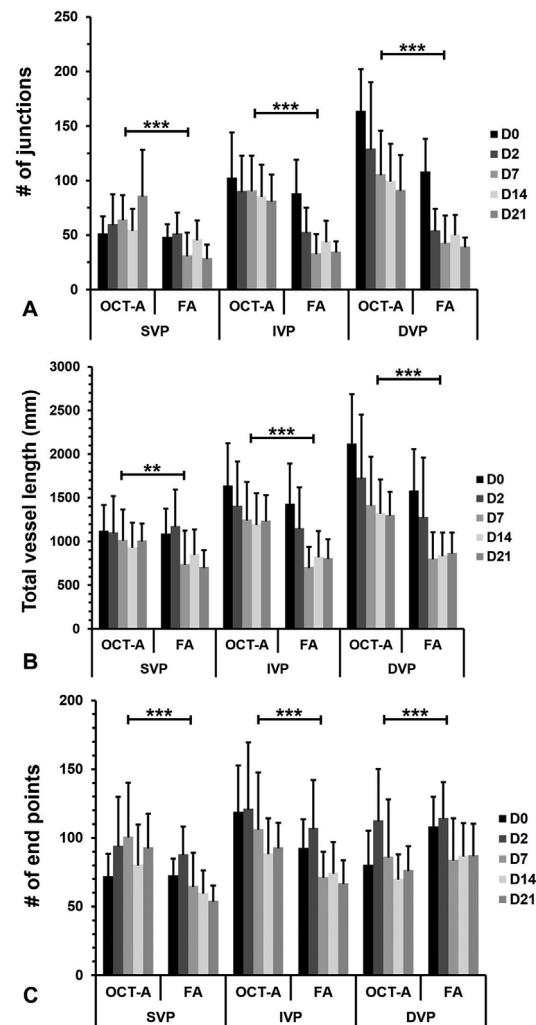


Fig. 6. Quantitative analysis of the retinal vascular network. Analysis of the mean number of vessel junctions (A), total vessel lengths (B) and total number of vessel end points (C) was performed by AngioTool software for the superficial, intermediate and deep vascular plexus compared for the OCT-A (n = 18) and FA (n = 20) in the laser lesion over all time points (D = day following initial laser treatment, D0 = before initial laser treatment). Statistical analysis using Wilcoxon signed rank test revealed significant differences at all time points for all three markers. (**P < 0.01; ***P < 0.001, Wilcoxon signed rank test).

projection artefacts from the SVP in deeper layers (represented as white color in FA images). Projection artefacts of superficial vessels were less in confocal microscopy but were also identified in the overlay (indicated by the reddish color) of colored OCT-A images (Figs. 8 and 9). Measurement of the IVP was difficult for FA and confocal microscopy in laser treated animals because of the relatively small number of vessels and the connecting feature of the intermediate vascular layer.

4. Discussion

This study demonstrates that in vivo OCT-A imaging can be accurately performed in small animals like rats. Detailed and high-contrast images of the retinal and choroidal vascular plexus can be visualized longitudinally without invasive dye injection. In comparison to FA, OCT-A is characterized by higher axial resolution and more accurate three-dimensional localization of retinal and choroidal vascular structures particularly in deep layers. Areas of laser-induced neovascularization were mainly detected in the area of the deep retinal vascular plexus, ONL, EZ and choroid.

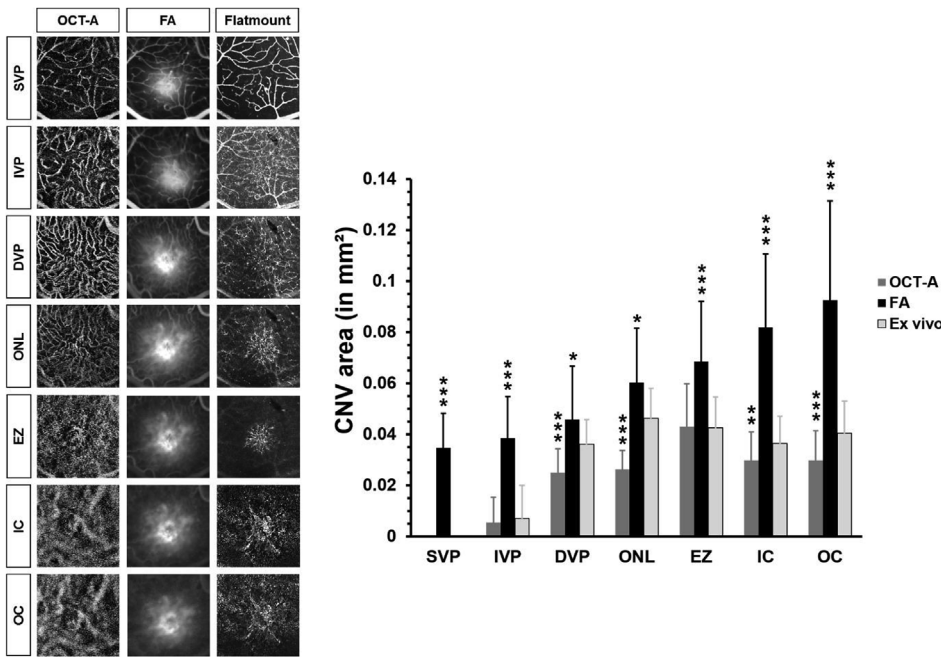


Fig. 7. Laser lesion imaging by OCT-A, FA and confocal microscopy. In vivo and ex vivo imaging by OCT-A (upper row, n = 18), FA (middle row, n = 20) or confocal microscopy (last row, n = 18) of retinal as well as RPE/choroidal/scleral flatmount preparations of the same laser lesion for the different retinal and choroidal layers at day 21 following the laser treatment. For histology, endothelial cells in flatmounts were stained with isolectin B4. Clearly, the same vascular structures were detected in the three image modalities in the SVP. In OCT-A and confocal microscopy images, CNV was mainly visible in the DVP, ONL and EZ but dye leakage covered neovascular structures in FA images. The area of CNV (in mm²) for OCT-A, FA and confocal microscopy images of retinal as well as RPE/choroidal/scleral flatmount preparations (ex vivo) were calculated (for D21). In total, CNV area in flatmounts was similar to OCT-A results and smaller compared to area of dye leakage by FA indicating the higher resolution achieved by OCT-A. Comparison of mean CNV area between OCT-A and histology of FA and histology were performed with the Wilcoxon signed rank test (*P < 0.05; **P < 0.01; ***P < 0.001, Wilcoxon signed rank test, OCT-A and FA results were compared to ex vivo results, respectively).

Using cSLO in rats, the tomographic in vivo analysis of retinal vessels was also possible by invasive FA. However, dye leakage at the site of CNV and staining of the surrounding tissue obscured the detailed visualization of neovascular structures in the retina and choroid to some degree. Due to this interference, CNV area was in general much more prominent and larger in FA images compared to OCT-A images while OCT-A images revealed detailed structural changes. Moreover, with FA no accurate segmentation of the different retinal layers was possible. In contrast, OCT-A and ex vivo confocal microscopy allow for a more precise detection of the normal and pathological vasculature with an overall better topographical resolution compared to FA. Particularly in the deep retinal vascular plexus a detailed, highly resolved and three-dimensional analysis of the neovascular (micro) structures was revealed by OCT-A in the animal model of laser-induced CNV. Interestingly, the laser injury was in the beginning visualized by OCT-A as a bright circle in the outer choroidal layer indicating a high ratio of blood flow in the choroidal vessels. It is interesting to note that by subthreshold laser treatment, slight structural changes in retinal and choroidal tissue (especially in the ONL, EZ and choroid) were still visible using OCT-A, although no leakage was detectable by FA. This might be another indication of the better resolution of OCT-A compared to conventional FA and reveals further insights in the laser-induced CNV model that were not detectable by dye leakage. With OCT-A, a precise measurement of the CNV area (induced by laser photocoagulation) was possible in the rat eye. McLenachan and coworkers showed, that the mouse DVP consists mostly of venous capillaries and the SVP of arterioles and precapillary arterioles (McLenachan et al., 2015). The IVP has been described as connecting layer between the SVP and the DVP with less density compared to the SVP and DVP (Campochiaro, 2015; Leahy et al., 2015; McLenachan et al., 2015; Uehara et al., 2018). The retinal network assessment showed similar results regarding the SVP in vessel density, number of vessel junctions, total vessel length and number of vessel end points for OCT-A and FA but not for IVP and DVP. Without previous laser treatment, vessel density for OCT-A showed a higher vessel density in the DVP compared to FA indicating the higher resolution in deeper layers achieved by OCT-A. In addition, through the invasive character of FA and obscuring the detailed visualization of neovascular structures in the retina by dye

leakage a decrease in vessel density in FA images for the intermediate and deep vasculature was observed. Therefore, a critical application of AngioTool is necessary for the analysis of dye leakage in FA images and the images should be considered individually during the examination. Nevertheless, AngioTool has proven to be a helpful method to quantify the retinal vascular network. Overall, these findings indicate the better resolution and more detailed visualization of the retinal blood vessels achieved by OCT-A compared to FA in deep layers in the animal model of laser-induced CNV. Moreover, the increase in vessel density in the IVP and DVP for OCT-A following the laser treatment over time might indicate the neovascular vessel growth in the area of CNV.

The correlation of the in vivo results by FA and OCT-A to ex vivo flatmounts confirmed the presence and spatial location of CNV areas. The size of CNV in (retinal and RPE/choroidal/scleral) flatmounts was similar to OCT-A results and smaller compared to the area of dye leakage in FA images. Difference between in vivo and ex vivo, analysis may occur due to shrinking artifact during tissue fixation and dehydration as previously reported (Jiao et al., 2013). In this study, we did not systematically assess the effect of tissue processing with regards to fixation time and other variations in the fixation protocol. Furthermore, discrepancies in vessel detection might be caused by the difference between assessment of flow velocity by in vivo imaging and the use of immunofluorescence markers (e.g. isolectin B4) in post-mortem tissue that could also stain nonpatent vessels in the early development of neovascularization.

In the applied animal model, CNV activity and new vessel formation was induced immediately following laser photocoagulation (Hoerster et al., 2012). Thereby, initial CNV development and active vessel formation continued only for several days up to few weeks with an increase in vessel number and overall CNV size (Edelman and Castro, 2000; Hoerster et al., 2012; Liu et al., 2013). Neovascular vessel growth from the choroid over various retinal layers up to the retinal nerve fiber layer took several days and progressed over a certain time. In the literature, time points of ongoing CNV development - in terms of increasing height, width or size of laser lesions - differ from 7 to 28 days following the initial laser treatment in the rodent model depending also on the examination method (OCT, cSLO, flatmounts and paraffin or frozen cross sections) (Campochiaro, 2015; Edelman and Castro, 2000;

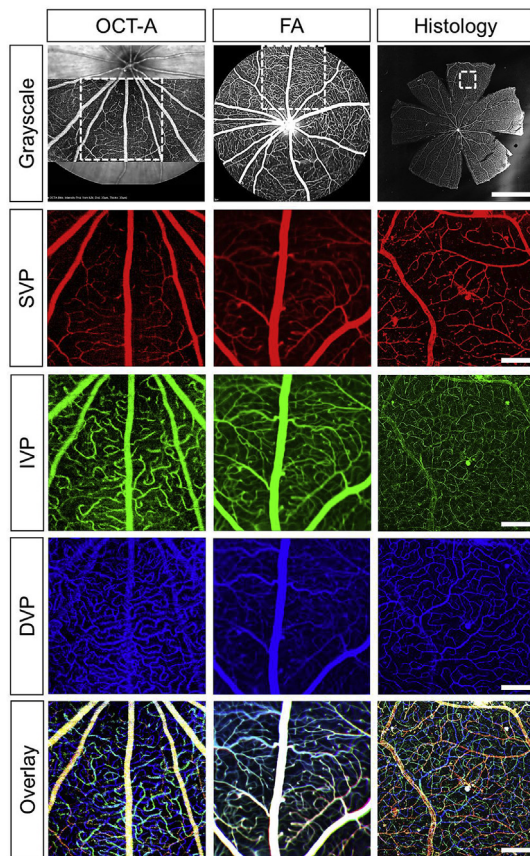


Fig. 8. Comparison of untreated rat retinae. OCT-A, FA and confocal microscopy images (grayscale, first row) of SVP, IVP and DVP from the intact rat retina. The vascular density of vessels forming the superficial (second row), intermediate (third row) and deep (fourth row) vascular plexus was visualized best in the confocal microscopy images of retinal flatmount preparations. In addition, the overlay of all three analyzed vascular plexus (fifth row) indicated the clear differentiation of the vascular network in the intact rat retina. However, the quantity of projection artefacts particular of the SVP was also visualized in the overlay. (Scale bars: histology first row = 0.4 cm and all other histology images = 200 μ m).

Jiao et al., 2013; Liu et al., 2013). In addition, CNV thickness and laser spot area were shown to decrease from day 1 to day 21 following the laser treatment in rats and mice (Hoerster et al., 2012; Liu et al., 2013). These findings are congruent to our results, which show a decrease in CNV area measurement investigated by OCT-A and conventional FA over time. However, other authors determined an increase of CNV thickness in paraffin or frozen sections and OCT from week 1 until week 3 post laser coagulation in rats (Jiao et al., 2013).

A well-described feature following rupture of the Bruch's membrane during laser injury is an increase in size, width and height of the choroid in the center of the laser lesion. This in vivo and ex vivo described feature is probably a result of laser photocoagulation in terms of swelling or edema effects. In paraffin and frozen sections, CNV area was found to extend from choroidal layers into the subretinal space resulting in a local displacement of different retinal layers. This displacement can also be detected topographically in vivo by OCT (Hoerster et al., 2012; Jiao et al., 2013; Liu et al., 2013). Hence, visualized changes of the retinal network by OCT-A following the initial laser injury could be also caused by choroidal displacements of retinal layers. Therefore, in vivo results by OCT-A in the animal model of laser-induced CNV should be carefully taken into consideration. Besides, there is an ongoing discussion in the literature about the correct interpretation and classification of clinical findings imaged by OCT-A (Coscas et al., 2015; Schmitz-Valckenberg et al., 2017). Thus, the new

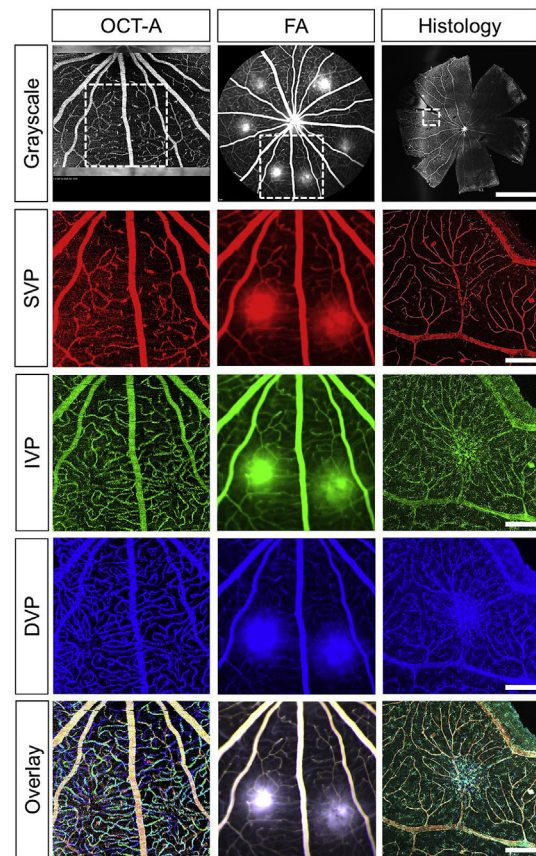


Fig. 9. Comparison of laser-treated rat retinae. OCT-A, FA and confocal microscopy images (grayscale, first row) of SVP, IVP and DVP from the laser treated rat retina. The vascular density of vessels forming the superficial (second row), intermediate (third row) and deep (fourth row) vascular plexus was visualized best in the confocal microscopy images. In addition, the overlay of all three analyzed vascular plexus (fifth row) indicated the clear differentiation of the vascular network and the dimension of laser lesion in the laser treated rat retina. However, the quantity of projection artefacts particular of the SVP was also visualized in the overlay. (Scale bars: histology first row = 0.4 cm and all other histology images = 200 μ m).

dimension of images generated by OCT-A requires careful and critical consideration in both basic and clinical research (Lindner et al., 2016).

Current limitations of our OCT-A imaging experiments in the rat model include that the lateral resolution of the OCT-A device was 11 μ m and thus small and adjacent capillaries might not be perfectly resolved. Generally, some projection artefacts and motion artefacts occurred during OCT-A. The projection artefacts were caused by the main retinal vessels shadowing in deeper layers whereas motion artefacts were traced back on breathing movements of the narcotized animal. In the presented study, artefacts occurred often in the region of the optic disc head (data not shown) and were mainly visualized in the superficial vascular plexus. In addition, the avascular ONL showed vascular structures due to projection artefacts of the deep vascular plexus. Dynamic phenomena like influx, pooling, leakage or staining are not detectable by OCT-A due to the non-invasive method (Supplement table 1). Nevertheless, dye leakage in FA clearly reveal the area of laser lesions and is a useful as well as worldwide established tool for drug treatment investigations (Campochiaro, 2015).

Especially the qualitative and quantitative analysis of the CNV area of FA angiograms is an essential part of the investigation of the improved and thus reducing effect on CNV. With the relatively new imaging method OCT-A, it is now possible to visualize neovascular structures in detail and thus provide additional information about the retinal and choroidal vasculature network. Thereby, the halo appearing

following the injection of fluorescein reveal the vascular leakage whereas OCT-A is visualizing the altered vasculature structure in the retina and choroid. Multimodal imaging approaches with a combined OCT-A and FA imaging tool in the rodent laser-induced CNV model can give a more refined insight in CNV development and progression which might be especially interesting for therapeutic interventional studies. Therefore, OCT-A could function as a useful and complementary tool combined with FA or even ICGA using the same multimodal imaging platform for the detailed investigation of neovascular structures in the laser-induced CNV animal model. In addition to the analysis of the area of CNV, it was shown that the volume of CNV in the animal model of laser-induced CNV can also be determined using histological cross sections or OCT-B scans (Berger et al., 2014; Ishida et al., 2017). Unfortunately, to the best of our knowledge, there are currently no specialized or automatic tools for such CNV volume assessment for FA and OCT-A images. Such 3D analysis of the laser-induced CNV might potentially reveal additional aspects of the development and progression of angiogenesis over time. For this purpose, novel applications based on deep learning methods could be used to predict the progression or extent of CNV over several retinal and choroidal layers.

The non-invasive method of OCT-A is of great advantage in animal studies because (intravenous) injections in small animals can be challenging. In addition, OCT-A permits a better insight into the retinal vasculature and into real-time morphological changes during the progression of neovascularization. A further advantage of OCT-A is the possibility to perform longitudinal investigations in the same animal at the same position in the eye (Supplement table 1). Until now, in vivo studied animals had to be sacrificed for histological correlation and thus no monitoring of the same animal over several days or weeks was possible. Therefore, OCT-A could be a very helpful tool in ophthalmological basic research projects bridging the gap between in vivo and ex vivo analysis and giving a more refined insight of vascular microstructure and possible age- or disease-related changes. Especially simultaneous in vivo imaging by OCT-A and the blue autofluorescence or near infrared autofluorescence channels could be an interesting tool for various research projects like investigations of potential new therapeutic targets for the treatment of exudative AMD (Meyer et al., 2017). In addition, non-invasive high resolution in vivo imaging of the topography and morphology of the retinal vasculature with adaptive optics (Domdei et al., 2017; Reiniger et al., 2017) in rodent models is possible (Schallek et al., 2013; Zawadzki et al., 2015).

In conclusion, OCT-A imaging may allow for a more precise spatial analysis of new blood vessel formation in CNV animal models as compared with FA. A longitudinal in vivo characterization of detailed CNV progression in rats by OCT-A could enable an overall better understanding of pathophysiological changes and possible treatment effects during neovascular vessel formation. In general, further investigations are necessary to evaluate OCT-A in general and especially in the model of laser-induced CNV and to characterize the CNV progression under anti-VEGF treatment in vivo. Overall, OCT-A is a reliable tool for detailed three-dimensional visualization of CNV formation and for accurately investigating the laser lesions in the rat model of laser-induced CNV.

Acknowledgments

The authors thank Claudine Strack for excellent technical assistance in histology and Heidelberg Engineering for providing the OCT-A device and technical support. We also would like to acknowledge Hannes Beckert with regard to the assistance of the Microscopy Core Facility of the Faculty of Medicine, University of Bonn and the Institute for Medical Biometry, Informatics, and Epidemiology, University of Bonn for statistical support.

Appendix A. Supplementary data

Supplementary data to this article can be found online at <https://doi.org/10.1016/j.exer.2019.04.002>.

Funding

This research did not receive any specific grant from funding agencies in the public, commercial, or not-for-profit sectors. Wolf M. Harmening received funding from the Emmy Noether Program of the German Research Foundation (DFG) Ha5323/5/1.

Authors disclosure

All: Centervue, Heidelberg Engineering GmbH, Optos, Carl-Zeiss Meditac AG; **Tim U. Krohne:** Alimera Sciences, Bayer, Novartis; **Frank G. Holz:** Acucela, Allergan, Bayer, Boehringer Ingelheim, Genentech, Merz, Novartis, Roche; **Steffen Schmitz-Valckenberg:** Genentech/Roche, Alcon/Novartis, Allergan, Bayer, Bioeq/Formycon

References

- Alnawaiseh, M., Rosentreter, A., Hillmann, A., Alex, A.F., Niekamper, D., Heiduschka, P., Pap, T., Eter, N., 2016. OCT angiography in the mouse: a novel evaluation method for vascular pathologies of the mouse retina. *Exp. Eye Res.* 145, 417–423.
- Atzpodien, E.-A., Jacobsen, B., Funk, J., Altmann, B., Silva Munoz, M.A., Singer, T., Gyger, C., Hasler, P., Maloca, P., 2015. Advanced clinical imaging and tissue-based biomarkers of the eye for toxicology studies in minipigs. *Toxicol. Pathol.* 1–16.
- Augustin, M., Wechdorn, M., Pfeiffenberger, U., Himmel, T., Fialova, S., Werkmeister, R.M., Hitzberger, C.K., Glosmann, M., Baumann, B., 2018. In vivo characterization of spontaneous retinal neovascularization in the mouse eye by multifunctional optical coherence tomography. *Investig. Ophthalmol. Vis. Sci.* 59, 2054–2068.
- Berger, A., Cavallero, S., Dominguez, E., Barbe, P., Simonutti, M., Sahel, J.A., Sennlaub, F., Raoul, W., Paques, M., Bemelmans, A.P., 2014. Spectral-domain optical coherence tomography of the rodent eye: highlighting layers of the outer retina using signal averaging and comparison with histology. *PLoS One* 9, e96494 96410.91371/journal.pone.0096494. eCollection 0092014.
- Bland, J.M., Altman, D.G., 1999. Measuring agreement in method comparison studies. *Stat. Methods Med. Res.* 8, 135–160.
- Campochiaro, P.A., 2015. Molecular pathogenesis of retinal and choroidal vascular diseases. *Prog. Retin. Eye Res.* 49, 67–81.
- Coscas, G.J., Lupidi, M., Coscas, F., Cagini, C., Souied, E.H., 2015. Optical coherence tomography angiography versus traditional multimodal imaging in assessing the activity of exudative age-related macular degeneration: a New Diagnostic Challenge. *Retina* 35, 2219–2228.
- Cunea, A., Meyer, J., Russmann, C., Licha, K., Welker, P., Holz, F.G., Schmitz-Valckenberg, S., 2014. In vivo imaging with a fundus camera in a rat model of laser-induced choroidal neovascularization. *Ophthalmologica* 231, 117–123.
- Dobi, E.T., Puliafito, C.A., Destro, M., 1989. A new model of experimental choroidal neovascularization in the rat. *Arch. Ophthalmol.* 107, 264–269.
- Domdei, N., Reiniger, J.L., Pfau, M., Charbel Issa, P., Holz, F.G., Harmening, W.M., 2017. [Histology of the living eye : noninvasive microscopic structure and functional analysis of the retina with adaptive optics]. *Ophthalmologie* 114, 206–214.
- Edelman, J.L., Castro, M.R., 2000. Quantitative image analysis of laser-induced choroidal neovascularization in rat. *Exp. Eye Res.* 71, 523–533.
- Fang, P.P., Lindner, M., Steinberg, J.S., Muller, P.L., Gliem, M., Charbel Issa, P., Krohne, T.U., Holz, F.G., 2016. [Clinical applications of OCT angiography]. *Ophthalmologie* 113, 14–22.
- Giannakaki-Zimmermann, H., Kokona, D., Wolf, S., Ebnetter, A., Zinkernagel, M.S., 2016. Optical coherence tomography angiography in mice: comparison with confocal scanning laser microscopy and fluorescein angiography. *Transl. Vis. Sci. Technol.* 5.
- Goody, R.J., Hu, W., Shafiee, A., Struharik, M., Bartels, S., Lopez, F.J., Lawrence, M.S., 2011. Optimization of laser-induced choroidal neovascularization in African green monkeys. *Exp. Eye Res.* 92, 464–472.
- Haefliger, J.A., Allagnat, F., Hamard, L., Le Gal, L., Meda, P., Nardelli-Haefliger, D., Genot, E., Alonso, F., 2017. Targeting Cx40 (Connexin40) expression or function reduces angiogenesis in the developing mouse retina. *Arterioscler. Thromb. Vasc. Biol.* 37, 2136–2146.
- Hoerster, R., Muether, P.S., Vierkotten, S., Schroder, S., Kirchhof, B., Fauser, S., 2012. In vivo and ex-vivo characterization of laser-induced choroidal neovascularization variability in mice. *Graefes Arch. Clin. Exp. Ophthalmol.* 250, 1579–1586.
- Ishida, T., Yoshida, T., Shinohara, K., Cao, K., Nakahama, K.I., Morita, I., Ohno-Matsui, K., 2017. Potential role of sirtuin 1 in Muller glial cells in mice choroidal neovascularization. *PLoS One* 12.
- Jiao, J., Mo, B., Wei, H., Jiang, Y.R., 2013. Comparative study of laser-induced choroidal neovascularization in rats by paraffin sections, frozen sections and high-resolution optical coherence tomography. *Graefes Arch. Clin. Exp. Ophthalmol.* 251, 301–307.
- Kim, Y., Hong, H.K., Park, J.R., Choi, W., Woo, S.J., Park, K.H., Oh, W.-Y., 2018. Oxygen-induced retinopathy and choroidopathy: in vivo longitudinal observation of vascular

- changes using OCTA. *Investig. Ophthalmol. Vis. Sci.* 59, 3932–3942.
- Lambert, V., Lecomte, J., Hansen, S., Blacher, S., Gonzalez, M.L., Struman, I., Sounni, N.E., Rozet, E., de Tullio, P., Foidart, J.M., Rakic, J.M., Noel, A., 2013. Laser-induced choroidal neovascularization model to study age-related macular degeneration in mice. *Nat. Protoc.* 8, 2197–2211.
- Leahy, C., Radhakrishnan, H., Weiner, G., Goldberg, J.L., Srinivasan, V.J., 2015. Mapping the 3D connectivity of the rat inner retinal vascular network using OCT angiography. *Investig. Ophthalmol. Vis. Sci.* 56, 5785–5793.
- Lindner, M., Fang, P.P., Steinberg, J.S., Domdei, N., Pfau, M., Krohne, T.U., Schmitz-Valckenberg, S., Holz, F.G., Fleckenstein, M., 2016. OCT angiography-based detection and quantification of the neovascular network in exudative AMD. *Investig. Ophthalmol. Vis. Sci.* 57, 6342–6348.
- Liu, T., Hui, L., Wang, Y.S., Guo, J.Q., Li, R., Su, J.B., Chen, J.K., Xin, X.M., Li, W.H., 2013. In-vivo investigation of laser-induced choroidal neovascularization in rat using spectral-domain optical coherence tomography (SD-OCT). *Graefes Arch. Clin. Exp. Ophthalmol.* 251, 1293–1301.
- Liu, W., Li, H., Shah, R.S., Shu, X., Linsenmeier, R.A., Fawzi, A.A., Zhang, H.F., 2015. Simultaneous optical coherence tomography angiography and fluorescein angiography in rodents with normal retina and laser-induced choroidal neovascularization. *Opt. Lett.* 40, 5782–5785.
- Maass, A., von Leithner, P.L., Luong, V., Guo, L., Salt, T.E., Fitzke, F.W., Cordeiro, M.F., 2007. Assessment of rat and mouse RGC apoptosis imaging in vivo with different scanning laser ophthalmoscopes. *Curr. Eye Res.* 32, 851–861.
- McLenachan, S., Magno, A.L., Ramos, D., Catita, J., McMenamin, P.G., Chen, F.K., Rakoczy, E.P., Ruberte, J., 2015. Angiography reveals novel features of the retinal vasculature in healthy and diabetic mice. *Exp. Eye Res.* 138, 6–21.
- Meyer, J., Cuneia, A., Sonntag-Bensch, D., Welker, P., Licha, K., Holz, F.G., Schmitz-Valckenberg, S., 2014 Sep 4. In vivo imaging of a new indocyanine green micelle formulation in an animal model of laser-induced choroidal neovascularization. *Investig. Ophthalmol. Vis. Sci.* 55 (10), 6204–6212. <https://doi.org/10.1167/iovs.13-13617>.
- Meyer, J.H., Cuneia, A., Licha, K., Welker, P., Sonntag-Bensch, D., Wafula, P., Dervedde, J., Fimmers, R., Holz, F.G., Schmitz-Valckenberg, S., 2016. In vivo imaging of fluorescent probes linked to antibodies against human and rat vascular endothelial growth factor. *Investig. Ophthalmol. Vis. Sci.* 57, 759–770.
- Meyer, J.H., Fang, P.P., Krohne, T.U., Harmening, W.M., Holz, F.G., Schmitz-Valckenberg, S., 2017. [Optical coherence tomography angiography (OCTA) in rats]. *Ophthalmologie* 114, 140–147.
- Nakagawa, K., Yamada, H., Mori, H., Toyama, K., Takahashi, K., 2018. Comparison between optical coherence tomography angiography and immunolabeling for evaluation of laser-induced choroidal neovascularization. *PLoS One* 13.
- Paques, M., Simonutti, M., Augustin, S., Goupille, O., El Mathari, B., Sahel, J.A., 2010. In vivo observation of the locomotion of microglial cells in the retina. *Glia* 58, 1663–1668.
- Park, J.R., Choi, W., Hong, H.K., Kim, Y., Jun Park, S., Hwang, Y., Kim, P., Joon Woo, S., Hyung Park, K., Oh, W.Y., 2016. Imaging laser-induced choroidal neovascularization in the rodent retina using optical coherence tomography angiography. *Investig. Ophthalmol. Vis. Sci.* 57, 15–18946.
- Reiniger, J.L., Domdei, N., Holz, F.G., Harmening, W.M., 2017. [Technical principles of adaptive optics in ophthalmology]. *Ophthalmologie* 114, 198–205.
- Schallek, J., Geng, Y., Nguyen, H., Williams, D.R., 2013. Morphology and topography of retinal pericytes in the living mouse retina using in vivo adaptive optics imaging and ex vivo Characterization Imaging retinal pericytes in the living mouse eye. *Investig. Ophthalmol. Vis. Sci.* 54, 8237–8250.
- Schmitz-Valckenberg, S., Brinkmann, C., Fleckenstein, M., Heimes, B., Liakopoulos, S., Spital, G., Holz, F., 2017. Fallstricke in der Netzhautbildgebung mittels optischer Kohärenztomographie. *Ophthalmologie* 114, 275–290.
- Schmitz-Valckenberg, S., Guo, L., Cheung, W., Moss, S.E., Fitzke, F.W., Cordeiro, M.F., 2010. [In vivo imaging of retinal cell apoptosis following acute light exposure]. *Ophthalmologie* 107, 22–29.
- Schmitz-Valckenberg, S., Guo, L., Maass, A., Cheung, W., Vugler, A., Moss, S.E., Munro, P.M., Fitzke, F.W., Cordeiro, M.F., 2008. Real-time in vivo imaging of retinal cell apoptosis after laser exposure. *Investig. Ophthalmol. Vis. Sci.* 49, 2773–2780.
- Shah, R.S., Soetikno, B.T., Yi, J., Liu, W., Skondra, D., Zhang, H.F., Fawzi, A.A., 2016. Visible-light optical coherence tomography angiography for monitoring laser-induced choroidal neovascularization in mice. *Investig. Ophthalmol. Vis. Sci.* 57, 15–18891.
- Soetikno, B.T., Shu, X., Liu, Q., Liu, W., Chen, S., Beckmann, L., Fawzi, A.A., Zhang, H.F., 2017. Optical coherence tomography angiography of retinal vascular occlusions produced by imaging-guided laser photocoagulation. *Biomed. Opt. Express* 8, 3571–3582.
- Spaide, R.F., Fujimoto, J.G., Waheed, N.K., 2015. Optical coherence tomography angiography. *Retina* 35, 2161–2162.
- Srinivasan, V.J., Radhakrishnan, H., 2013. Total average blood flow and angiography in the rat retina. *J. Biomed. Opt.* 18, 076025.
- Uehara, H., Lesuma, T., Stocking, P., Jensen, N., Kumar, S.R., Zhang, M.A., Choi, S., Zhang, X., Archer, B., Carroll, L., Ambati, B.K., 2018. Detection of microvascular retinal changes in type I diabetic mice with optical coherence tomography angiography. *Exp. Eye Res.* 27 30516–30515.
- Wigg, J.P., Zhang, H., Yang, D., 2015. A quantitative and standardized method for the evaluation of choroidal neovascularization using MICRON III fluorescein angiograms in rats. *PLoS One* 10, e0128418 0128410.0121371/journal.pone.0128418. eCollection 0122015.
- Zawadzki, R.J., Zhang, P., Zam, A., Miller, E.B., Goswami, M., Wang, X., Jonnal, R.S., Lee, S.H., Kim, D.Y., Flannery, J.G., Werner, J.S., Burns, M.E., Pugh Jr., E.N., 2015. Adaptive-optics SLO imaging combined with widefield OCT and SLO enables precise 3D localization of fluorescent cells in the mouse retina. *Biomed. Opt. Express* 6, 2191–2210 2110.1364/BOE.2196.002191. eCollection 002015, Jun 002191.
- Zudaire, E., Gambardella, L., Kurcz, C., Vermeren, S., 2011. A computational tool for quantitative analysis of vascular networks. *PLoS One* 6, 16.